Graphitic Carbon Quantum Dots Modified Nickel Cobalt Sulfide as Cathode Materials for Alkaline Aqueous Batteries

Yirong Zhu[1], Jingying Li[1], Xiaoru Yun[1], Ganggang Zhao[2], Peng Ge[2], Guoqiang Zou[2], Yong Liu[3], Hongshuai Hou[2] ✉, Xiaobo Ji[2]

✉ Hongshuai Hou, hs-hou@csu.edu.cn

[1] College of Metallurgy and Material Engineering, Hunan University of Technology, Zhuzhou 412007, People's Republic of China

[2] College of Chemistry and Chemical Engineering, Central South University, Changsha 410083, People's Republic of China

[3] State Key Lab of Powder Metallurgy, Central South University, Changsha 410083, People's Republic of China

HIGHLIGHTS

- The scalable graphitic carbon quantum dots (CQDs) are obtained with a high yield of more than 50%.

- The CQDs are utilized to synthesize novel NS-CQDs/NiCo$_2$S$_4$ composite which shows enhanced electrochemical properties.

- The assembled novel alkaline aqueous battery delivers superior electrochemical performances.

ABSTRACT Carbon quantum dots (CQDs) as a new class of emerging materials have gradually drawn researchers' concern in recent years. In this work, the graphitic CQDs are prepared through a scalable approach, achieving a high yield with more than 50%. The obtained CQDs are further used as structure-directing and conductive agents to synthesize novel N,S-CQDs/NiCo$_2$S$_4$ composite cathode materials, manifesting the enhanced electrochemical properties resulted from the synergistic effect of highly conductive N,S-codoped CQDs offering fast electronic transport and unique micro-/nanostructured NiCo$_2$S$_4$ microspheres with Faradaic redox characteristic contributing large capacity. Moreover, the nitrogen-doped reduced graphene oxide (N-rGO)/Fe$_2$O$_3$ composite anode materials exhibit ultrahigh specific capacity as well as significantly improved rate property and cycle performance originating from the high-capacity prism-like Fe$_2$O$_3$ hexahedrons tightly wrapped by highly conductive N-rGO. A novel alkaline aqueous battery assembled by these materials displays a specific energy (50.2 Wh kg^{-1}), ultrahigh specific power (9.7 kW kg^{-1}) and excellent cycling performance with 91.5% of capacity retention at 3 A g^{-1} for 5000 cycles. The present research offers a valuable guidance for the exploitation of advanced energy storage devices by the rational design and selection of battery/capacitive composite materials.

KEYWORDS Energy storage; Alkaline aqueous batteries; Carbon quantum dot; Nickel cobalt sulfide
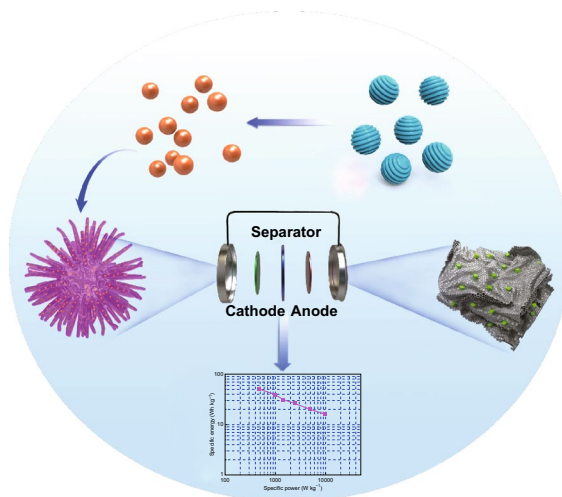
1 Introduction

Carbon quantum dots (CQDs), as a novel type of zero-dimensional (0D) carbon materials with ultrasmall sizes less than 10 nm, have been extensively applied in fluorescence, bioimaging, biosensing, photocatalysis and photovoltaics owing to their unique advantages such as quantum confinement and edge effects [1–4]. In particular, the application of CQDs in energy storage has gradually attracted researchers' attention in recent years [5–7]. In the early research, the reduced carbon quantum dots (rCQDs)/RuO$_2$ composites have been obtained as ultrafast supercapacitor electrode materials for the first time, where rCQDs are utilized as conductive agents to boost the electrical conductivity of electrode materials, enhancing the supercapacitive properties, especially rate capability [8]. Since this reported pioneering work, more researches about such CQDs-based energy storage materials as supercapacitors, lithium/sodium ion batteries and fuel cell have been explored [9–14], which indicates that these upcoming CQDs-based electrode materials present a great prospect as superior energy storage materials. Nevertheless, the utilization of CQDs as electrode materials is much less reported compared to the conventional carbon materials; hence, it shows a great potential to further explore them.

Currently, the methods for the synthesis of CQDs are usually classified into "top-down" and "bottom-up" types. The former is usually breaking down large-size carbon materials into CQDs, including arc discharge, electrochemical exfoliation, hydrothermal technique and chemical oxidation synthesis [15–18], whereas the latter is usually preparing CQDs from molecular precursors, such as combustion/thermal decomposition method, supported synthesis and microwave pyrolysis synthetic route [19–21]. However, these approaches for the synthesis of CQDs still face major challenges, such as a low yield (usually lower than 10%), complicated processes, poor reproducibility and electronic conductivity [1]. In our previous study, graphitic CQDs were obtained via chemical oxidation synthesis route utilizing nano-graphite powders (~30 nm) as precursors, and a relatively low yield of less than 20% was acquired [8, 10]. Hou et al. obtained non-graphitic CQDs through a facile and scalable solution growth method by mixing NaOH and acetone together, and an ultrahigh yield with gram level was achieved. However, the resulted CQDs presented low electronic conductivity, leading to the poor electrochemical properties [12]. From the perspective of practical application for energy storage electrode materials, it is crucially important to develop a scalable approach for synthesizing CQDs with a high yield, low cost and high electrical conductivity.

Besides, another major challenge for CQDs is that they are apt to aggregate and stack together, which results in a rapid decrease in their specific surface areas and kinetic behaviors, thus worsening the electrochemical properties of CQDs [22]. These obstacles above prevent their utilization as excellent energy storage electrode materials. The most effective method to solve the aggregation is to employ them as composite materials. Recently, ternary metal oxides/sulfides have attracted extensive interests because of their higher electrical conductivity and richer electrochemical activity than those of the corresponding binary metal oxides/sulfides, which have been explored as potential cathode materials for alkaline aqueous batteries [23–28]. Among them, NiCo$_2$S$_4$ is seen as the most prospective candidate for future utilization in such energy storage as supercapacitors and lithium ion batteries. To further enhance its comprehensive electrochemical performances, an effective way is to design various unique micro-/nanostructured NiCo$_2$S$_4$, and the enhanced electrochemical properties have been reported by researchers in the literature [29–33]. Another good way is to introduce carbon materials to prepare the composite electrode materials, leading to the enhanced electrochemical properties to some extent. Currently, the most reported carbon materials are graphene and carbon nanotubes, demonstrating decent electrochemical properties, but their high cost seriously prevents the practical application [34, 35]. Therefore, it is very emergent to exploit novel and cheap carbon materials for the fabrication of superior composite electrode materials.

As discussed above, the scalable graphitic CQDs were first synthesized with a high yield of more than 50% utilizing highly conductive Super P powders as precursors. Then, the CQDs were employed as both structure-directing and conductive agents to prepare new N,S-codoped CQDs-decorated urchin-like NiCo$_2$S$_4$ microspheres for the first time. In comparison with the pure NiCo$_2$S$_4$ electrode, the N,S-CQDs/NiCo$_2$S$_4$ composite electrode, when for the first time used as cathode for alkaline aqueous batteries, exhibits enhanced electrochemical properties with a high specific capacity of 124.4 mAh g^{-1} at 2 A g^{-1}, exceptional capacity retention of 77.3% at 50 A g^{-1} in comparison with 2 A g^{-1} and excellent

cycling property with 97.9% of initial capacity retention at 3 A g^{-1} for 5000 cycles. Meanwhile, the N-rGO-wrapped prism-like Fe$_2$O$_3$ hexahedrons composite anode materials are obtained, which manifest substantially enhanced electrochemical performances with an ultrahigh specific capacity (249.6 mAh g^{-1} at 1 A g^{-1}) as well as greatly enhanced rate property and cycling life compared with those of the pristine Fe$_2$O$_3$ electrode. A novel N,S-CQDs/NiCo$_2$S$_4$//N-rGO/Fe$_2$O$_3$ alkaline aqueous battery fabricated by these materials achieves a specific energy (50.2 Wh kg^{-1}) and ultrahigh specific power (9,700 W kg^{-1}) with excellent cycle property (91.5% of capacity retention for 5000 cycles). The encouraging results display the enormous potential of the new alkaline aqueous battery as highly promising energy storage system for potentially practical applications.

2 Experimental Section

2.1 Synthesis of CQDs

CQDs were obtained by a scalable chemical oxidation approach. Super P powders (1 g, purchased from Sigma-Aldrich) were first added into concentrated H$_2$SO$_4$/HNO$_3$ mixed solution (80 mL, v/v, 3:1) and then sonicated for 1 h. The resulting mixture was refluxed for 24 h. Subsequently, the mixture was further neutralized with Na$_2$CO$_3\cdot$10H$_2$O, and the pH was controlled at 7.0. After further dialysis and vacuum-drying, the final CQDs powders were obtained.

2.2 Synthesis of N,S-CQDs/NiCo$_2$S$_4$ Composite Materials

The N,S-CQDs/NiCo$_2$S$_4$ composite materials were synthesized by a one-step hydrothermal approach. Firstly, CQDs powders (22.3 mg) were dissolved in H$_2$O/ethanol mixed solution (60 mL, v/v, 1:1) and agitated for 10 min. Subsequently, NiCl$_2\cdot$6H$_2$O (0.06952 g) and CoCl$_2\cdot$6H$_2$O (0.13919 g) were added into the obtained mixture and stirred for 20 min. Then, thioacetamide (0.13185 g) was further introduced into the above mixture. After continual agitating for another 20 min, the as-resulted mixed solution was transferred into a stainless steel autoclave lined with PTFE (100 mL) and hydrothermally treated at 180 °C for 24 h. The products were obtained by alternate centrifuging with H$_2$O and ethanol for three times and further

vacuum-dried overnight at 70 °C. For comparison, the pure NiCo$_2$S$_4$ was synthesized by the similar method only without adding CQDs powders in this preparation process.

2.3 Synthesis of N-rGO/Fe$_2$O$_3$ Composite Materials

The N-rGO/Fe$_2$O$_3$ composite materials were prepared by a facile hydrothermal approach. Firstly, graphite oxide (GO, 40 mg, purchased from XFNANO) was dissolved in H2O solution (30 mL) and sonicated for 1 h. Then, FeCl3·6H2O (0.5406 g) was dissolved in H2O solution (15 mL) and stirred for 10 min. The as-resulted FeCl$_3$ aqueous solution was added into the GO solution and sonicated for 30 min. Meanwhile, urea (0.6006 g) was dissolved in H2O solution (15 mL) and magnetically stirred for 10 min. Furthermore, the resulting urea solution was slowly introduced into the above mixture under strong agitation. After stirring for 30 min, the as-obtained mixture was transferred into a stainless steel autoclave lined with PTFE (100 mL) and subjected to hydrothermal reaction at 180 °C for 10 h. Lastly, the products were obtained by alternately centrifuging with H$_2$O and ethanol for three times and further vacuum-dried overnight at 70 °C. For comparison, the pure Fe$_2$O$_3$ was synthesized by the similar method only in the absence of GO in this preparation process.

2.4 Materials Characterization

X-ray diffraction (XRD) analysis was implemented on an X-ray diffractometer (Rigaku D/max 2550 VB$^+$). Raman spectra were executed on a Raman spectrometer (Labram-010). X-ray photoelectron spectroscope (XPS) analysis was conducted on a photoelectron spectrometer (K-Alpha). FESEM images, EDS and elemental mappings were captured on a field emission scanning electron microscopy (FESEM, MIRA3). Transmission electron microscope (TEM) images, HRTEM images and SAED patterns were obtained on a transmission electron microscopy (JEM-2100F). TG curves were recorded from a thermal analysis instrument (NETZSCH STA449C). N$_2$ adsorption/desorption isotherms were acquired on a BET specific surface area analyzer (BELSORP-miniII).

2.5 Electrochemical Measurements

To fabricate the working electrodes for electrochemical tests, 70 wt% of electroactive material, 20 wt% of Super P and 10 wt% of PVDF with NMP as solvent were adequately mixed to obtain an uniform slurry. Afterward, the resulting slurry was dipped into Ni foam current collector, which was pretreated based on our previous work [10], and dried in a vacuum oven at 70 °C overnight. Finally, the as-fabricated electrodes were further pressed at 10 MPa. The electrochemical properties of the single electrode were conducted by employing a typical three-electrode cell with platinum foil, Hg/HgO and 2 M KOH solution as counter electrode, reference electrode and electrolyte, respectively. The alkaline aqueous coin battery (CR 2016) was further assembled by utilizing N,S-CQDs/NiCo$_2$S$_4$ as cathode, N-rGO/Fe$_2$O$_3$ as anode, glassy fibrous material as separator and 2 M KOH solution as electrolyte. The electrochemical tests such as CV, GCD and EIS for both single electrode and alkaline aqueous device were executed on an electrochemical workstation (CHI 760E).

3 Results and Discussion

3.1 Preparation Processes of the CQDs and the Composite Cathode and Anode

The synthetic processes of the graphitic CQDs, the N,S-CQDs/NiCo$_2$S$_4$ composite cathode and N-rGO/Fe$_2$O$_3$ composite anode are demonstrated in Fig. 1. First, the graphitic CQDs are prepared through a scalable mixed-acid chemical oxidation approach using the industrialized, cheap and highly conductive Super P powders as precursors. The obtained CQDs achieve a high yield of more than 50%, which is far higher than that prepared by most of previous work reported in the literature [1, 8, 10, 36, 37], demonstrating the great prospect for their potentially practical application. Afterward, the resulting CQDs are further employed as structure-directing and conductive agents to prepare novel N,S-codoped CQDs-decorated urchin-like NiCo$_2$S$_4$ microspheres composite cathode materials via a one-step hydrothermal approach, in which thioacetamide is used as precipitant to generate the NiCo$_2$S$_4$ and codoped agent to achieve nitrogen and
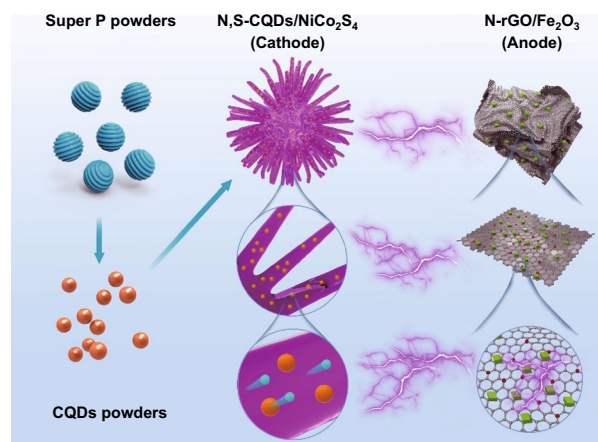

Fig. 1 Schematic illustration of the synthetic processes of the CQDs, the N,S-CQDs/NiCo$_2$S$_4$ composite cathode and N-rGO/Fe$_2$O$_3$ composite anode

sulfur codoping into the CQDs. In this process, the CQDs are not only utilized as structure-directing agents to induce the formation of nanorods-assembled urchin-like composite microsphere structure, but also served as conductive agents to improve the electrical conductivity of the composite cathode materials. Meanwhile, the N-doped rGO-wrapped prism-like Fe$_2$O$_3$ hexahedrons composite anode materials are prepared by a facile hydrothermal synthetic route, where urea serves as precipitant to generate the Fe$_2$O$_3$ and acts as doped agent to achieve nitrogen doping into the GO. The Fe$_2$O$_3$ hexahedrons are tightly wrapped by the N-rGO sheets, and the close contact between the Fe$_2$O$_3$ hexahedrons and the N-rGO sheets can improve the electrochemical kinetic behavior and structural stability of the composite anode materials.

3.2 Physicochemical Characterization of CQDs

Figure 2a shows the digital photograph of the industrial Super P powders, and their FESEM images (Fig. S1) reveal that the Super P powders display nanoparticles-like morphology with a size of about 50 nm. As observed from the digital photograph (Fig. S2a), the Super P powders are insoluble in H$_2$SO$_4$/HNO$_3$ mixed solution after the treatment of sonication. However, the digital photograph (Fig. S2b) reveals that the obtained CQDs are highly soluble in H$_2$O solution, and also the resulted CQDs aqueous solution does
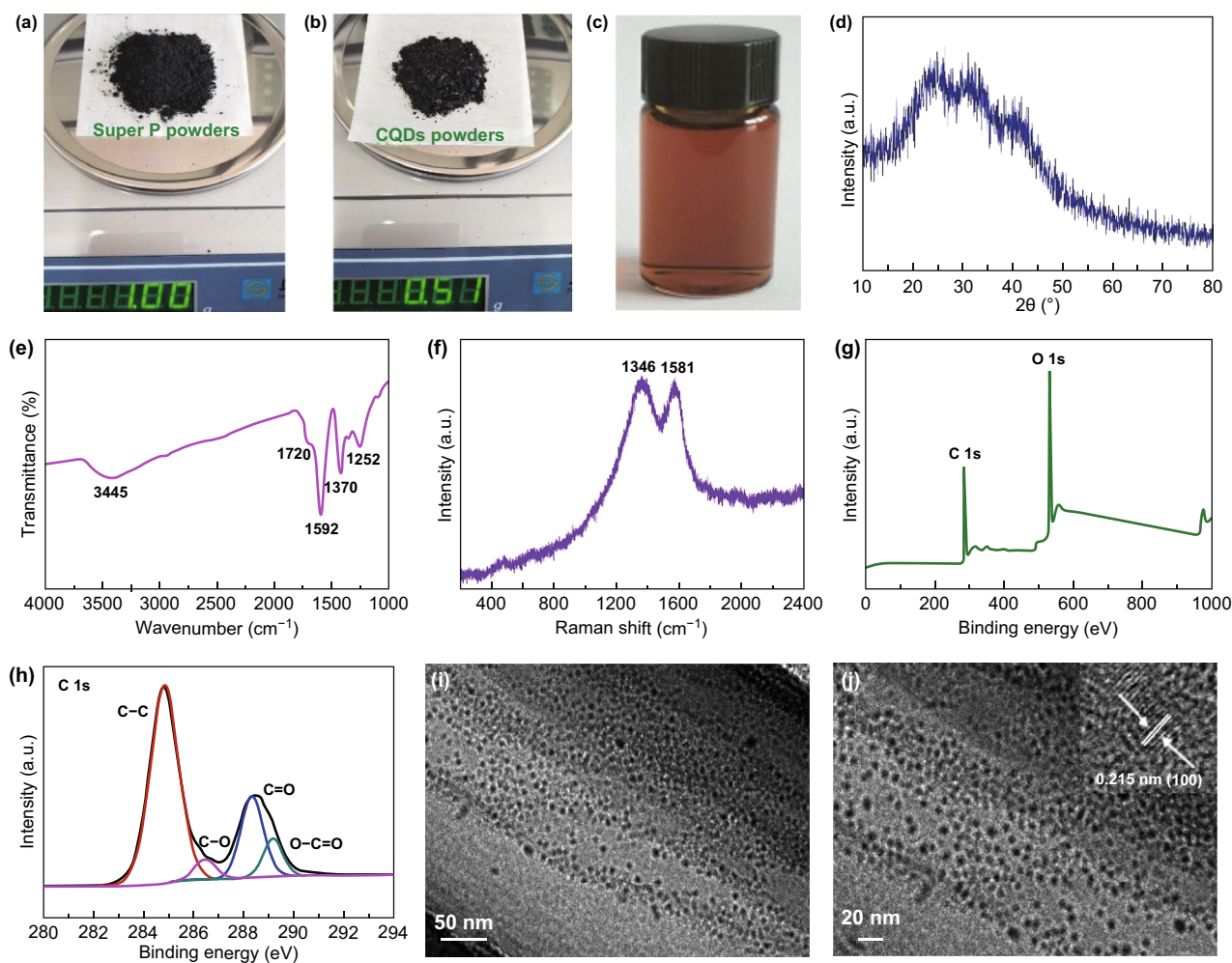
Fig. 2 Digital photograph of **a** Super P powders, **b** CQDs powders, and **c** CQDs aqueous solution with a concentration of 1 mg mL^{-1}. **d** XRD pattern, **e** FTIR spectroscopy, **f** Raman spectroscopy, **g** XPS survey spectrum, **h** high-resolution C 1 s spectrum, **i, j** TEM images and HRTEM image (inset of Fig. 2j) of CQDs

not show any change after 6 months at ambient temperature as manifested in Fig. 2c, suggesting their high stability. Figure 2b is the digital photograph of the final obtained CQDs powders, and the yield is up to 51%. Thus, the scalable synthesis of CQDs with a high yield, together with the advantages of employing a cheap and industrial carbon source, renders them being potential candidate electrode materials for large-scale storage application.

Figure 2d illustrates the XRD pattern of CQDs, and the broad peak of CQDs at around 25° corresponds to (002) plane of the disordered graphite carbon resulting from the strong acid etching [38]. Also, no other peak such as

inorganic salts is observed, indicating the high purity of CQDs. FTIR spectrum (Fig. 2e) reveals that the main peaks at 3445, 1720, 1592, 1370 and 1252 cm^{-1} are well fitted to the C–OH, C = O, C = C, C–H and C–O–C bonds [8, 39], respectively, and the existence of these bonds shows that the CQDs are functionalized with the abundant oxygen-containing surface groups, which is particular in favor of the construction of composite materials by the utilization of the functionalized CQDs. Raman spectroscopy (Fig. 2f) was used to further characterize the structure of CQDs. The two obvious peaks at 1346 and 1581 cm^{-1} belong to the D-band and G-band of CQDs, which are attributed to the disordered

carbon and ordered graphitic structure, respectively [40]. XPS was undertaken to characterize the elemental composition and carbon bonds of CQDs, as presented in Fig. 2g, h. The four peaks at 284.8, 286.5, 288.4 and 289.2 eV in the spectrum of C1s (Fig. 2h) are, respectively, ascribed to the C–C, C–O, C=O and O–C=O bonds, which accord well with FTIR analysis results [12]. Figure 2i, j exhibits the TEM images of the as-obtained CQDs, and it is clear that the as-prepared CQDs are monodisperse with the uniform distribution in the range of 5–8 nm. As exhibited in the inset of Fig. 2j, the HRTEM image manifests the lattice fringe of 0.215 nm, which accords well with the (100) plane of graphitic carbon, proving the formation of graphitic CQDs.

3.3 Physicochemical and Electrochemical Characterizations of the Cathode Materials

The morphology and microstructure of the as-resulted N,S-CQDs/NiCo$_2$S$_4$ composite were examined by FESEM, TEM, HRTEM, EDS and elemental mappings. As demonstrated in Fig. 3a–c, the FESEM images show that the composite presents the urchin-like microsphere structure with a size of about 3 μm, and the microspheres are composed of numerous nanorods. The superior micro-/nanostructured morphology of the composite is achieved when compared to that of the pristine NiCo$_2$S$_4$ where only the microspheres with irregular and larger sizes are obtained as exhibited in Fig.
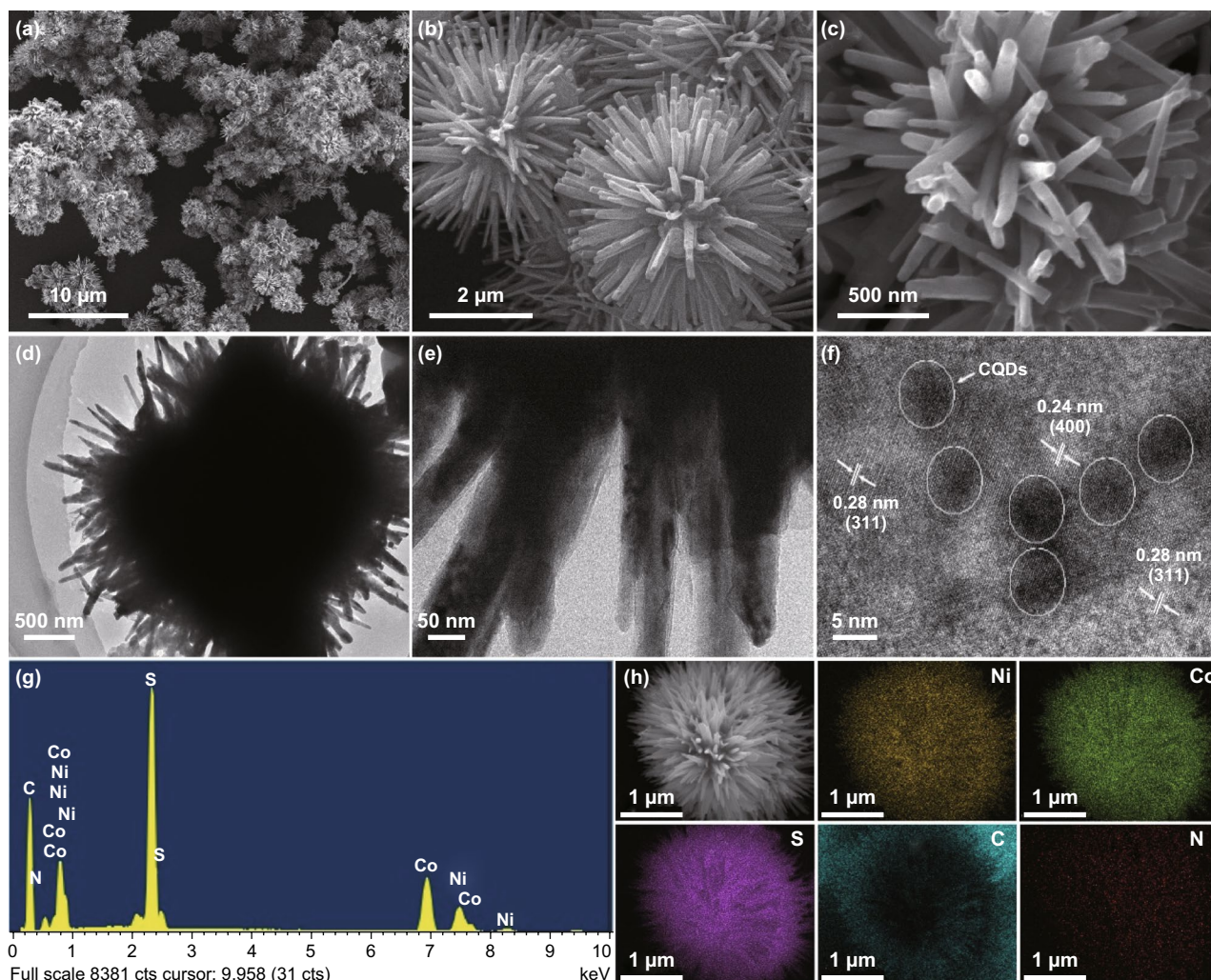

Fig. 3 **a–c** FESEM images, **d, e** TEM images, **f** HRTEM image, **g** EDS spectrum and **h** corresponding elemental mappings of Ni, Co, S, C and N elements of the N,S-CQDs/NiCo$_2$S$_4$ composite

S3, which is ascribed to the induced role of CQDs during the formation process of the composite. The micro-/nanostructured morphology of the composite was further surveyed by TEM and HRTEM. The TEM images (Fig. 3d, e) reveal the nanorods-assembled urchin-like microsphere structure with a size of approximately 3 μm, which is well matched with the FESEM images. As displayed in Fig. 3f, the HRTEM image of the composite shows that the CQDs are well combined with $NiCo_2S_4$ to obtain the uniform composite structure. Moreover, the HRTEM image exhibits the lattice fringes of 0.28 and 0.24 nm, which, respectively, accord well with the (311) and (400) planes of $NiCo_2S_4$. In addition, the EDS analysis (Fig. 3g) and corresponding elemental mappings

(Fig. 3h) show the existence of Ni, Co, S, C and N, suggesting the formation of N,S-CQDs/$NiCo_2S_4$ composite.

XRD was employed to examine the phase and structure of the pristine $NiCo_2S_4$ and N,S-CQDs/$NiCo_2S_4$ composite, and the results are exhibited in Fig. 4a. The main diffraction peaks of the pristine $NiCo_2S_4$ and N,S-CQDs/$NiCo_2S_4$ composite can be clearly observed from the XRD patterns, which all well correspond to the $NiCo_2S_4$ (JCPDS Card No. 20-0782), suggesting that the structure of the composite is not changed in the combination of N,S-CQDs and $NiCo_2S_4$. However, it is hard to notice the peak of N,S-CQDs due to the relatively low content and weak diffraction peak intensity. Raman spectra were used to further characterize the structure of the pristine $NiCo_2S_4$ and N,S-CQDs/
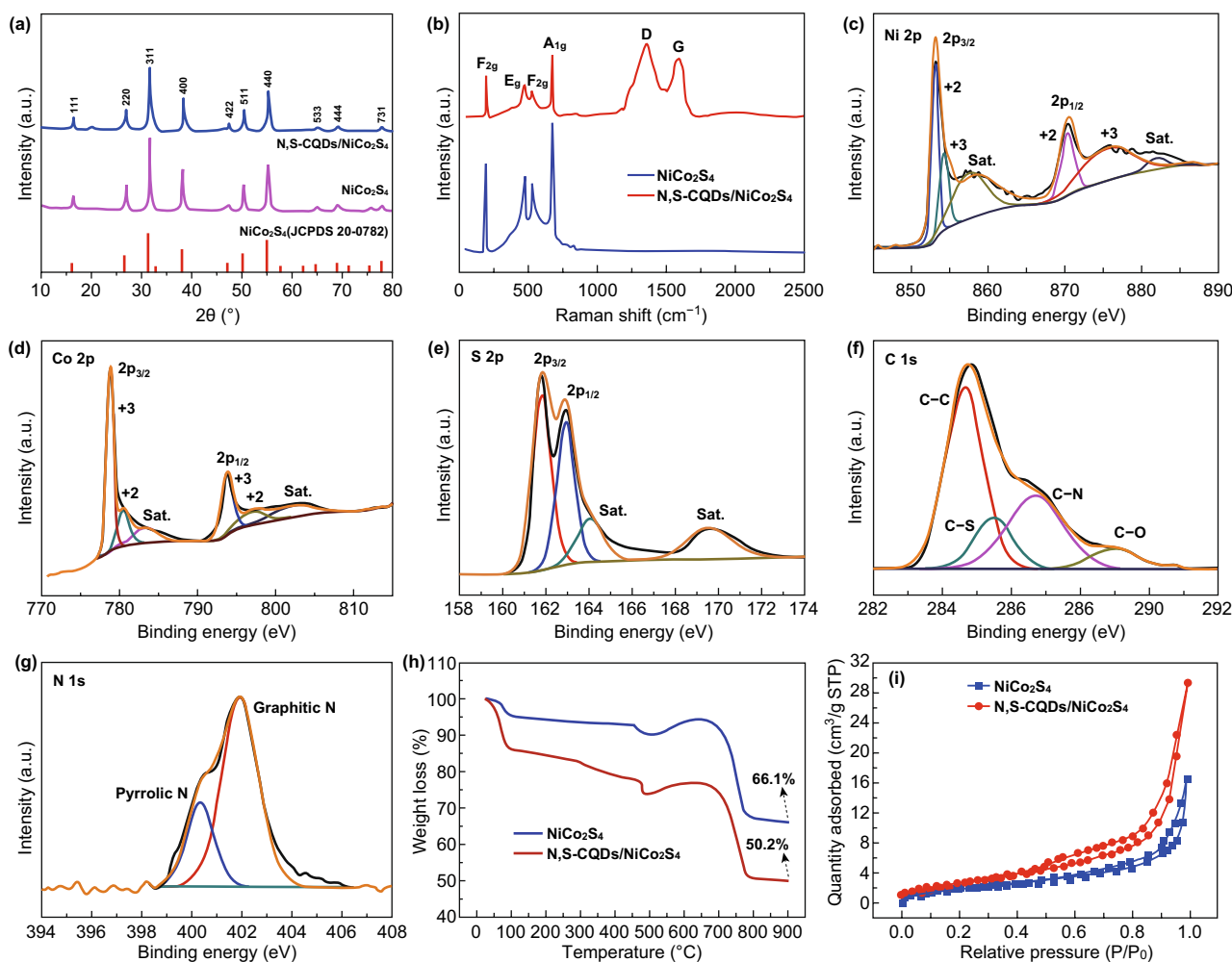
Fig. 4 **a** XRD patterns, **b** Raman spectra of the pristine $NiCo_2S_4$ and N,S-CQDs/$NiCo_2S_4$ composite. XPS high-resolution spectra of **c** Ni 2p, **d** Co 2p, **e** S 2p, **f** C 1s and **g** N 1s of the N,S-CQDs/$NiCo_2S_4$ composite. **h** TG curves and **i** Nitrogen adsorption–desorption isotherms of the N,S-CQDs/$NiCo_2S_4$ composite

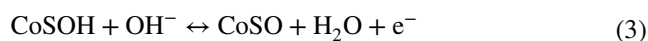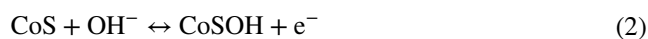NiCo$_2$S$_4$ composite (Fig. 4b). Four peaks all can be seen for the pristine NiCo$_2$S$_4$ and N,S-CQDs/NiCo$_2$S$_4$ composite, which correspond to two F_{2g} (191 and 524 cm^{-1}), one E_g (472 cm^{-1}) and one A_{1g} (675 cm^{-1}) Raman modes of NiCo$_2$S$_4$ [29]. Moreover, the D-band (disordered carbon) and G-band (ordered graphitic carbon) situated at 1356 and 1590 cm^{-1} are characteristic Raman modes of carbon, which are seen from the Raman spectroscopy of the N,S-CQDs/NiCo$_2$S$_4$ composite.

XPS was further undertaken to study the elemental composition and valence state of the as-synthesized N,S-CQDs/NiCo$_2$S$_4$ composite, as presented in Fig. 4c–g. The survey spectrum (Fig. S4) demonstrates the coexistence of Ni, Co, S, C, O and N. Figure 4c, d, respectively, exhibits the spectra of Ni 2p and Co 2p. The two peaks situated at 853.04 and 870.44 eV are indexed to Ni^{2+}, and another two peaks situated at 854.24 and 876.04 eV are indexed to Ni^{3+}, respectively [41]. Similarly, the two peaks situated at 780.54 and 797.24 eV can be ascribed to Co^{2+}, and another two peaks situated at 778.74 and 793.79 eV can be attributed to Co^{3+}, respectively [41]. The S 2p spectrum presented in Fig. 4e represents two main peaks situated at 161.9 and 163.0 eV, which are, respectively, ascribed to the S^{2-} in low coordination at the surface and the metal–sulfur bonds [34]. For the C 1 s spectrum (Fig. 4f), four main peaks situated at 284.64, 285.49, 286.70 and 289.04 eV are, respectively, assigned to the C–C, C–S, C–N and C–O bonds [24], and the as-formed C–S and C–N bonds indicate that the nitrogen and sulfur elements are successfully codoped into CQDs. Furthermore, Fig. 4g displays the N 1 s spectrum with two main peaks situated at 400.3 and 401.9 eV, which correspond to the pyrrolic N and graphitic N [42]. Based on these results above, the XPS characterization exhibits the coexistence of Ni, Co, S, C and N elements in the N,S-CQDs/NiCo$_2$S$_4$ composite.

To further determine the composition of the prepared N,S-CQDs/NiCo$_2$S$_4$ composite, the thermogravimetric analysis (TGA) was executed in air atmosphere from ambient temperature to 900 °C as demonstrated in Fig. 4h. The TG curves of the pristine NiCo$_2$S$_4$ and N,S-CQDs/NiCo$_2$S$_4$ composite both show two apparent weight losses and one obvious weight gain. For the N,S-CQDs/NiCo$_2$S$_4$ composite, the first weight loss before 500 °C is more obvious than that of the pristine NiCo$_2$S$_4$, which results from the burning of CQDs and the loss of physically adsorbed and crystalline water. The second apparent weight gain between 500 and 650 °C is attributed to the oxidation of NiCo$_2$S$_4$ to NiSO$_4$

and CoSO$_4$, and the third evident weight loss in the temperature range of 650 and 800 °C is ascribed to the further burning of CQDs as well as the decomposition of NiSO$_4$ and CoSO$_4$ to stable NiO and CoO as reported in the literature [43–45]. From the different weight losses of the pristine NiCo$_2$S$_4$ and N,S-CQDs/NiCo$_2$S$_4$ composite, it is deduced that the content of CQDs in composite is about 15.9 wt%. N$_2$ adsorption/desorption test was employed to research the specific surface area of the pristine NiCo$_2$S$_4$ and N,S-CQDs/NiCo$_2$S$_4$ composite, as presented in Fig. 4i. The N,S-CQDs/NiCo$_2$S$_4$ composite manifests a greater specific surface area (27.2 m^2 g^{-1}) than that of the pristine NiCo$_2$S$_4$ (14.9 m^2 g^{-1}), which contributes to the enhancement of electrochemical properties.

The electrochemical performances of the NiCo$_2$S$_4$ and N,S-CQDs/NiCo$_2$S$_4$ electrodes were investigated in a three-electrode configuration with 2 M KOH solution as electrolyte. Figure 5a shows the comparison of the CV curves of NiCo$_2$S$_4$ and N,S-CQDs/NiCo$_2$S$_4$ electrodes at 20 mV s^{-1} in the potential range of 0 to 0.6 V. The two electrodes both manifest strong and broad redox peaks in the CV curves, implying the combination of Faradaic battery and double-layer capacitive behavior. The Faradaic battery behavior is derived from reversible redox reactions of Ni^{2+}/Ni^{3+} and Co^{2+}/Co^{3+}/Co^{4+} according to Eqs. 1–3 [34]:

$$NiS + OH^- \leftrightarrow NiSOH + e^- \tag{1}$$

$$CoS + OH^- \leftrightarrow CoSOH + e^- \tag{2}$$

$$CoSOH + OH^- \leftrightarrow CoSO + H_2O + e^- \tag{3}$$

Ex situ XRD measurement was utilized to characterize the phase change of the N,S-CQDs/NiCo$_2$S$_4$ composite during different electrochemical steps, as exhibited in Fig. 5d. The alteration in reflections indicates the phase change in the charge–discharge process and verifies that Faradaic redox reactions occur in bulk, demonstrating the feature of Faradaic battery. Furthermore, it is clear that the area of CV curve of the N,S-CQDs/NiCo$_2$S$_4$ electrode is greater than that of the NiCo$_2$S$_4$ electrode, revealing that the N,S-CQDs/NiCo$_2$S$_4$ electrode shows higher specific capacity. Figure 5b, c displays the CV curves of the NiCo$_2$S$_4$ and N,S-CQDs/NiCo$_2$S$_4$ electrodes at different scan rates, respectively. The N,S-CQDs/NiCo$_2$S$_4$ electrode manifests a smaller peak position shift than that of the NiCo$_2$S$_4$ electrode as the scanning speed increases from 5 to 100 mV s^{-1}, suggesting
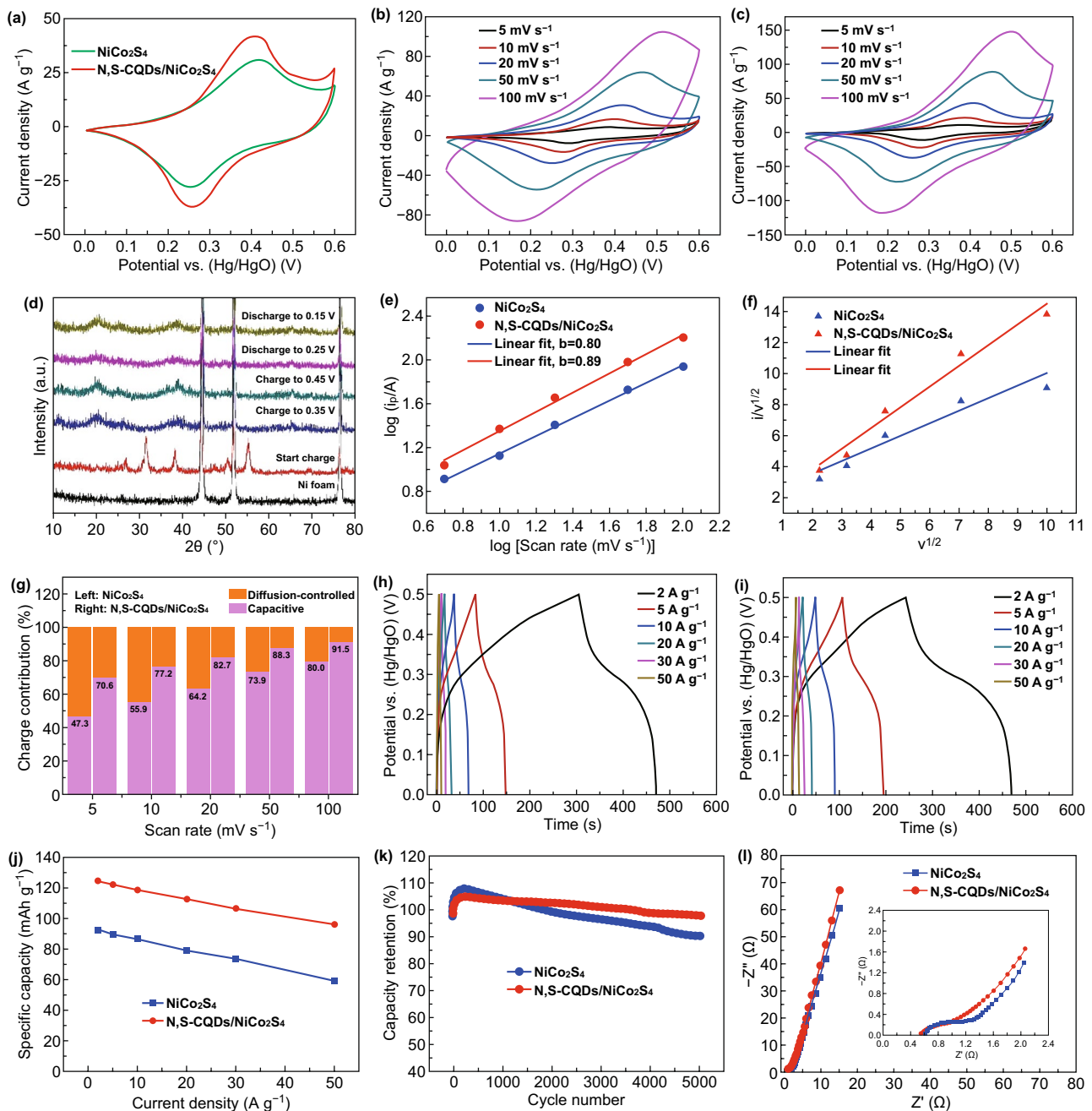
Fig. 5 **a** Comparison of CV curves of the pristine NiCo$_2$S$_4$ and N,S-CQDs/NiCo$_2$S$_4$ electrodes at 20 mV s^{-1}. CV curves at various scan rates of the **b** pristine NiCo$_2$S$_4$ and **c** N,S-CQDs/NiCo$_2$S$_4$ electrodes. **d** Ex-situ XRD measurement of the N,S-CQDs/NiCo$_2$S$_4$ electrode during different electrochemical steps. **e** The fitting lines of log (scan rate, mV s^{-1})-log (i_p, A), **f** $i/v^{1/2}$–$v^{1/2}$, and **g** the charge contribution of the pristine NiCo$_2$S$_4$ and N,S-CQDs/NiCo$_2$S$_4$ electrodes. GCD curves at various current densities of the **h** pristine NiCo$_2$S$_4$ and **i** N,S-CQDs/NiCo$_2$S$_4$ electrodes. **j** The rate performances, **k** cycling performances, and **l** EIS plots of the pristine NiCo$_2$S$_4$ and N,S-CQDs/NiCo$_2$S$_4$ electrodes

that the composite electrode has lower polarization, better conductivity and faster electrochemical kinetic. To further explore the difference of the electrochemical behaviors of the NiCo$_2$S$_4$ and N,S-CQDs/NiCo$_2$S$_4$ electrodes, the

quantitative analysis was conducted based on the mechanism of charge storage. The relationship of the peak currents (i_p) and scan rates is expressed as $I = av^b$ shown in Fig. 5e [26], where the b-value of 0.5 and 1 suggests the

diffusion-controlled and surface capacitive processes of the electrochemical reaction, respectively. The calculated b-value of the $NiCo_2S_4$ and N,S-CQDs/$NiCo_2S_4$ electrodes is, respectively, 0.80 and 0.89, indicating a mixed behavior of diffusion-controlled and surface capacitive processes. The higher b-value of the N,S-CQDs/$NiCo_2S_4$ electrode signifies more surface capacitive behaviors. Furthermore, the result is further verified by the quantitative calculation of the contribution of the diffusion-controlled and surface capacitive charge, which is obtained from the following equation [26]: $i(V) = k_1v + k_2v^{1/2}$, in which k_1v represents the surface capacitive current and $k_2v^{1/2}$ denotes the diffusion-controlled current. The fitted lines of the $i/v^{1/2}$ to $v^{1/2}$ of the two electrodes are presented in Fig. 5f, and the values of the slope and intercepts, respectively, represent the constants of k_1 and k_2. The charge contributions of the $NiCo_2S_4$ and N,S-CQDs/$NiCo_2S_4$ electrodes are manifested in Fig. 5g, and it is visible that the N,S-CQDs/$NiCo_2S_4$ electrode displays larger capacitive contribution ratio than that of the $NiCo_2S_4$ electrode at all scan rates, which reasonably elucidates why the N,S-CQDs/$NiCo_2S_4$ electrode possesses faster electrochemical kinetic than that of the $NiCo_2S_4$ electrode.

Figure 5h, i exhibits the GCD curves of the $NiCo_2S_4$ and N,S-CQDs/$NiCo_2S_4$ electrodes at different current densities in the potential window of 0–0.5 V, respectively. The GCD curves of the N,S-CQDs/$NiCo_2S_4$ electrode present a better symmetry than that of the pristine $NiCo_2S_4$ electrode, signifying that the composite electrode has lower resistance and higher rate performance. The specific capacities of the two electrodes are calculated according to the GCD curves, as exhibited in Fig. 5j. The specific capacity of the N,S-CQDs/$NiCo_2S_4$ electrode is, respectively, 124.4, 122.4, 118.6, 112.8, 106.4 and 96.1 mAh g^{-1} at 2, 5, 10, 20, 30 and 50 A g^{-1}, which is better than that of the $NiCo_2S_4$ electrode (from 92.8 mAh g^{-1} at 2 A g^{-1} to 59.1 mAh g^{-1} at 50 A g^{-1}). Correspondingly, the N,S-CQDs/$NiCo_2S_4$ electrode manifests a greater capacity retention of 77.3% at 50 A g^{-1} than that of the $NiCo_2S_4$ electrode (63.7% of capacity retention at 50 A g^{-1}). The improved specific capacity and rate performance of the N,S-CQDs/$NiCo_2S_4$ electrode originate from the positive synergistic effect between highly conductive N,S-CQDs with the capacitive feature and high-capacity $NiCo_2S_4$ with Faradaic characteristic. Note that the specific capacity and rate performance of the as-obtained N,S-CQDs/$NiCo_2S_4$ composite are comparable or even higher than those of nickel cobalt sulfide-based composite as reported in the literature [46–53]. The cycling property of the $NiCo_2S_4$ and N,S-CQDs/$NiCo_2S_4$ electrodes was surveyed by the repeated GCD tests at 5 A g^{-1} in the potential range of 0–0.5 V over 5000 cycles, as exhibited in Fig. 5k. The specific capacity of the two electrodes increases in the first hundreds of cycles due to the gradually sufficient activation process and then reduces with a gradual decline as the increasing cycles [23, 26]. After 5000 cycles, the N,S-CQDs/$NiCo_2S_4$ electrode manifests a better cycle property with 97.9% of the initial capacity retention than that of the $NiCo_2S_4$ electrode (90.3%), revealing the excellent cycling stability of the as-resulted composite electrode. Additionally, the EIS test was utilized to illustrate the superior electrochemical behaviors, which was implemented in the frequency range of 0.01 Hz to 100 kHz at the open-circuit potential (Fig. 5l). The Nyquist plot consists of the intercept and depressed semicircle in the high-frequency region as well as the slope line in the low-frequency region [54, 55]. The N,S-CQDs/$NiCo_2S_4$ electrode displays smaller intercept, lower semicircle diameter and higher slope value than those of the $NiCo_2S_4$ electrode, indicating the lower resistance and better electrical conductivity of the composite electrode, leading to the improved electrochemical properties.

3.4 Physicochemical and Electrochemical Characterizations of the Anode Materials

Figures 6a and S5 display the FESEM images of the N-rGO/Fe_2O_3 composite, and it is clearly observed that the prism-like Fe_2O_3 hexahedrons are tightly wrapped by the N-rGO layers, suggesting the close contact between the Fe_2O_3 hexahedrons and the N-rGO sheets. Such a composite structure can increase their contact and hinder the agglomeration of Fe_2O_3 and N-rGO, thereby promoting the improvement of electrochemical activity and stability of the composite. TEM study demonstrated in Figs. 6b and S6 was employed to verify the formation of the N-rGO/Fe_2O_3 composite, and the prism-like Fe_2O_3 hexahedrons with a size of about 100 nm were well combined with N-doped rGO sheets to form the composite. It is noted that the pristine Fe_2O_3 displays the morphology of prism-like hexahedrons from the FESEM and TEM images demonstrated in Figs. S7 and S8, indicating that the morphology of the composite is not altered in the combination of Fe_2O_3 and N-rGO. As exhibited in Fig. 6c, the HRTEM
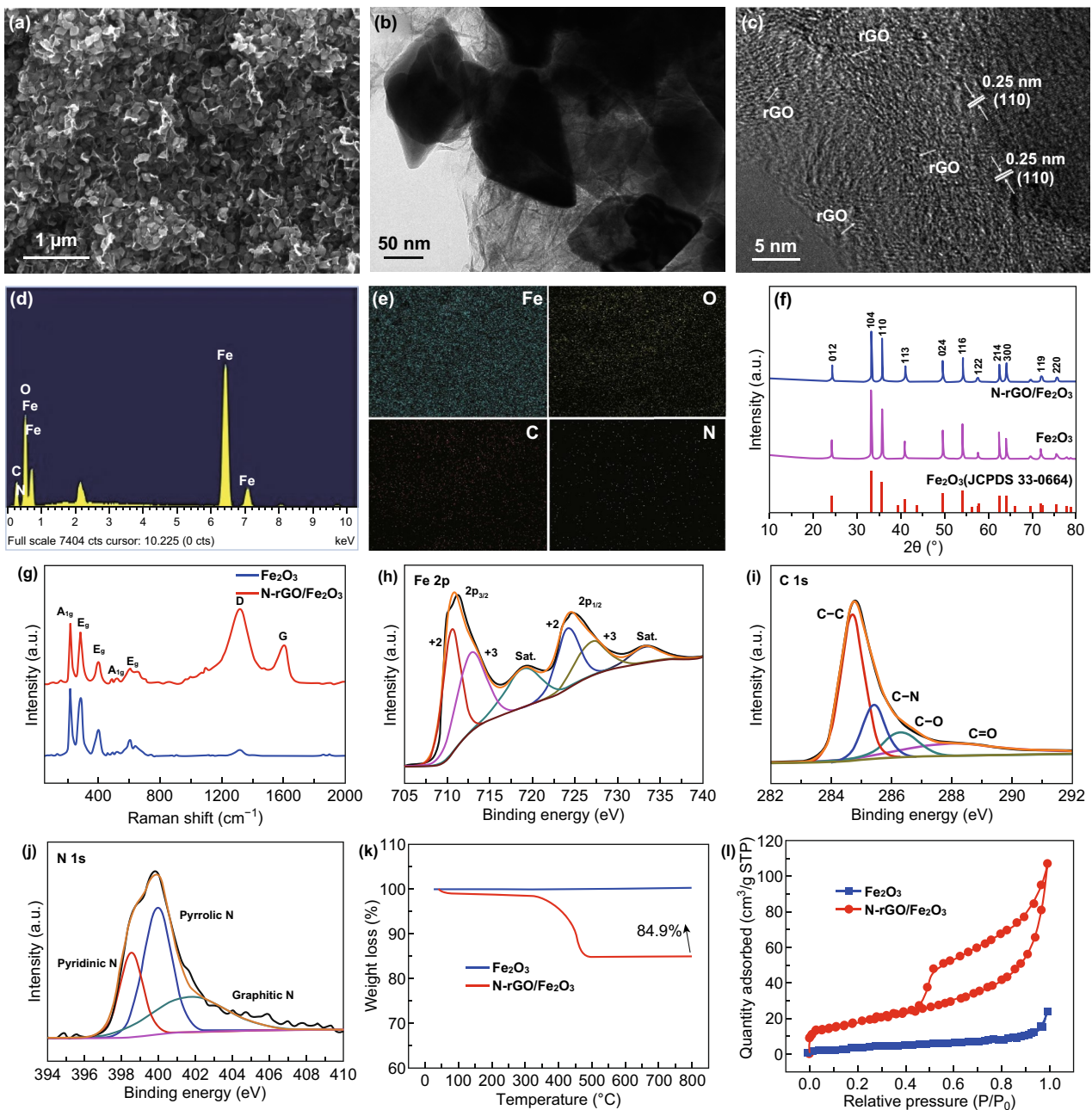
Fig. 6 **a** FESEM image, **b** TEM image, **c** HRTEM image, **d** EDS spectrum and **e** corresponding elemental mappings of Fe, O, C and N elements of the N-rGO/Fe$_2$O$_3$ composite. **f** XRD patterns and **g** Raman spectra of the pristine Fe$_2$O$_3$ and N-rGO/Fe$_2$O$_3$ composite. XPS high-resolution spectra of **h** Fe 2p, **i** C 1 s and **j** N 1s of the N-rGO/Fe$_2$O$_3$ composite. **k** TG curves and **l** nitrogen adsorption–desorption isotherms of the N-rGO/Fe$_2$O$_3$ composite

image indicates the presence of crumpled N-rGO, and the lattice fringe of 0.25 nm matches well with the (110) crystal plane of Fe$_2$O$_3$. EDS and the corresponding elemental mappings were utilized to examine the elemental composition and distribution of the N-rGO/Fe$_2$O$_3$ composite.

The EDS spectrum (Fig. 6d) verifies the existence of Fe, O, C, and N in the composite, and elemental mappings (Fig. 6e) reveal that these elements are uniformly distributed throughout the composite.

XRD was utilized to further characterize the structure and phase of the pristine Fe_2O_3 and N-rGO/Fe_2O_3 composite (Fig. 6f). The XRD patterns show the strong diffraction peaks of the pristine Fe_2O_3 and N-rGO/Fe_2O_3 composite, which are both well fitted to the Fe_2O_3 (JCPDS Card No. 33-0664). Note that the characteristic peaks of rGO cannot be observed in the XRD pattern of the composite, which results from the weak and broad peak and low rGO content in composite. Raman spectra were used to further examine the structure of the pristine Fe_2O_3 and N-rGO/Fe_2O_3 composite (Fig. 6g). Five peaks all can be seen from the Raman spectra of the pristine Fe_2O_3 and N-rGO/Fe_2O_3 composite, which are attributed to two A_{1g} (218 and 483 cm^{-1}) and three E_g (283, 399, and 601 cm^{-1}) Raman modes of Fe_2O_3 [56]. Besides, two typical peaks situated at 1320 and 1596 cm^{-1} are assigned to the D-band and G-band, respectively, further suggesting that the Fe_2O_3 is successfully combined with the N-rGO to form the composite.

XPS was further applied to explore the elemental composition and valence state of the obtained N-rGO/Fe_2O_3 composite, as presented in Fig. 6h–j. The survey spectrum (Fig. S9) demonstrates the existence of Fe, O, C and N in the N-rGO/Fe_2O_3 composite. For the Fe 2p spectrum (Fig. 6h), the peaks situated at 710.5 and 724.1 eV are assigned to Fe^{2+}, and the peaks situated at 712.8 and 726.8 eV are well fitted to Fe^{3+} [57]. As for the C 1 s spectrum shown in Fig. 6i, the peaks located at 284.7, 285.4, 286.3 and 288.1 eV correspond to the C–C, C–N, C–O and C=O bonds [58], and the as-formed C–N bond implies that the nitrogen element is well doped into rGO. Furthermore, the N 1 s spectrum manifested in Fig. 6j reveals that the peaks located at 398.5, 399.9 and 401.6 eV correspond well with the pyridinic N, pyrrolic N and graphitic N [59]. Thus, the XPS analysis further proves the formation of the N-rGO/Fe_2O_3 composite.

The content of GO in N-rGO/Fe_2O_3 composite was determined by TGA test, which is executed in air atmosphere from room temperature to 800 °C as demonstrated in Fig. 6k. From the TGA curves, almost no weight loss of the pristine Fe_2O_3 can be seen in the whole temperature range, suggesting the high stability of the Fe_2O_3 in air, while an obvious weight loss of the N-rGO/Fe_2O_3 composite can be observed between 350 and 470 °C due to the burning of rGO. Apparently, the rGO content in the N-rGO/Fe_2O_3 composite is deduced to be about 15.1 wt%. As exhibited in Fig. 6l, the BET specific surface areas of the pristine Fe_2O_3 and N-rGO/

Fe_2O_3 composite are obtained by the nitrogen adsorption/desorption test. Benefiting from the introduction of N-rGO in composite, the N-rGO/Fe_2O_3 composite displays a far greater BET specific surface area (66.8 m^2 g^{-1}) than that of the pristine Fe_2O_3 (13.8 m^2 g^{-1}), and thus, it is expected that the N-rGO/Fe_2O_3 composite can present excellent electrochemical performances.

The electrochemical properties of the pristine Fe_2O_3 and N-rGO/Fe_2O_3 composite were also studied in a three-electrode cell with 2 M KOH solution as electrolyte. Figure 7a presents the comparison of CV curves of the Fe_2O_3 and N-rGO/Fe_2O_3 electrodes at 20 mV s^{-1} within the potential range of − 1.2 to− 0.2 V. Apparently, the composite electrode manifests a distinctly greater area of CV curve than that of the Fe_2O_3 electrode, implying that the composite electrode shows much larger specific capacity than that of the pristine Fe_2O_3 electrode. The substantially improved specific capacity of the composite electrode is ascribed to the positive synergistic effect of the double-layer capacitive behavior of N-rGO and Faradaic redox reaction of Fe_2O_3. Ex situ XRD test (Fig. 7d) was also used to investigate the phase change of the N-rGO/Fe_2O_3 composite during different electrochemical steps. The observed change in reflections reveals the phase change in the charge/discharge process and confirms the occurring of Faradaic redox reactions, further demonstrating the typical battery characteristic. In comparison with the Fe_2O_3 electrode, the N-rGO/Fe_2O_3 electrode shows a smaller potential difference of the anodic and cathodic peak (ΔE_P), implying the lower resistance and better kinetic behavior. Figure 7b, c displays the CV curves of the Fe_2O_3 and N-rGO/Fe_2O_3 electrodes, respectively, and no distinct distortion can be noticed with the increasing scanning speed from 5 to 50 mV s^{-1}. Figure 7e, f exhibits the GCD curves of the Fe_2O_3 and N-rGO/Fe_2O_3 electrodes at various current densities in the potential range between− 1 and − 0.2 V, respectively. The calculated specific capacity of the N-rGO/Fe_2O_3 electrode (Fig. 7g) is, respectively, 249.6, 228.4, 206.7, 174.2, 130.4 and 96.2 mAh g^{-1} at 1, 2, 3, 5, 10 and 20 A g^{-1}, which is much better than that of the Fe_2O_3 electrode (from 109.1 at 1 A g^{-1} to 21.8 mAh g^{-1} at 20 A g^{-1}). Moreover, the specific capacity of the N-rGO/Fe_2O_3 electrode is not only far higher than that of carbon-based anode materials, but also comparable to or even larger than that of most Fe_2O_3-based anode
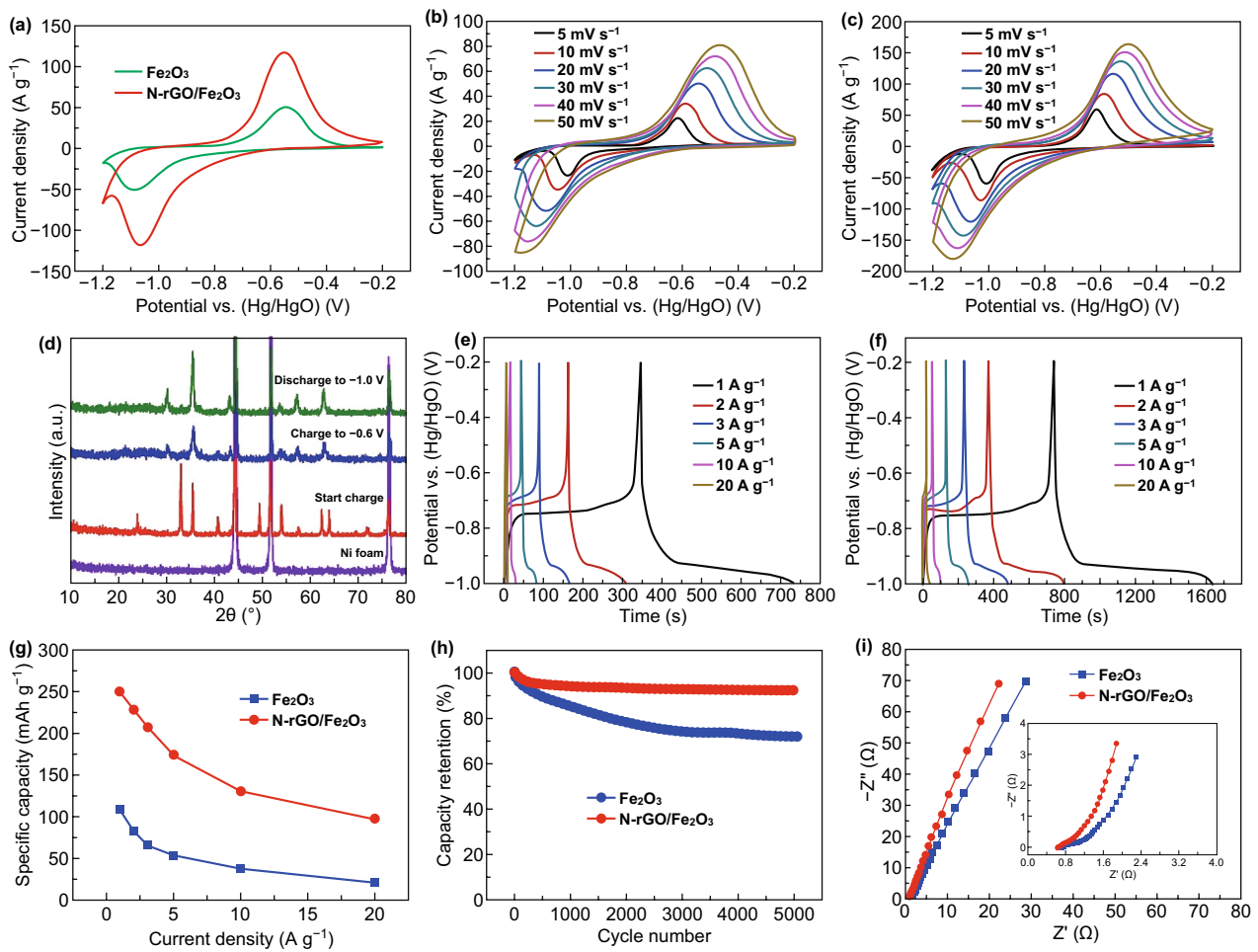
Fig. 7 **a** Comparison of CV curves of the pristine Fe_2O_3 and N-rGO/Fe_2O_3 electrodes at 20 mV s^{-1}. CV curves at various scan rates of the **b** pristine Fe_2O_3 and **c** N-rGO/Fe_2O_3 electrodes. **d** Ex-situ XRD measurement of the N-rGO/Fe_2O_3 electrode during different electrochemical steps. GCD curves at various current densities of the **e** pristine Fe_2O_3 and **f** N-rGO/Fe_2O_3 electrodes. **g** The rate performances, **h** cycling performances, and **i** EIS plots of the pristine Fe_2O_3 and N-rGO/Fe_2O_3 electrodes

materials reported in the literature [56–58, 60–64]. The cycle property of the Fe_2O_3 and N-rGO/Fe_2O_3 electrodes was further compared by the repeated GCD tests at 3 A g^{-1} over 5000 cycles, as manifested in Fig. 7h. The N-rGO/Fe_2O_3 electrode manifests a better cycle stability with 92.1% capacity retention than that of the Fe_2O_3 electrode (71.8%) after 5000 cycles, suggesting that the unique N-rGO-tightly-wrapped Fe_2O_3 composite structure can prevent the agglomeration of Fe_2O_3 and N-rGO and alleviate the volume change in the repeated charging-discharging processes, leading to the improvement of cycle performance. Moreover, the EIS measurement was taken, and the Nyquist plots are demonstrated in Fig. 7i. The N-rGO/Fe_2O_3 electrode shows smaller intercept and semicircle diameter in the high-frequency region as well

as higher slope value in the low-frequency region than those of the Fe_2O_3 electrode. Therefore, the results well demonstrate why the N-rGO/Fe_2O_3 electrode presents improved electrochemical performances in comparison with the Fe_2O_3 electrode.

3.5 Electrochemical Characterizations of the N,S-CQDs/NiCo$_2$S$_4$//N-rGO/Fe$_2$O$_3$ Alkaline Aqueous Battery

To further clarify the superior electrochemical properties of the N,S-CQDs/NiCo$_2$S$_4$ and N-rGO/Fe_2O_3 composites, a novel alkaline aqueous battery was assembled by, respectively, employing the two composites as the cathode and
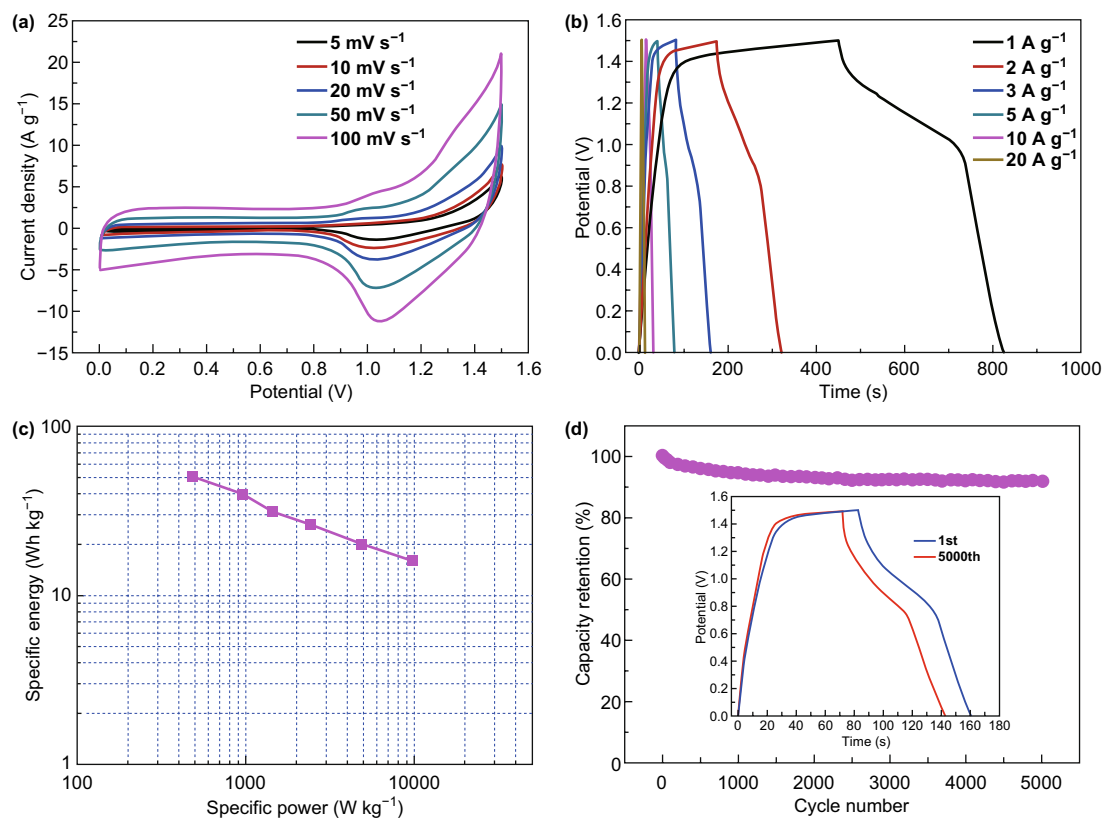
Fig. 8 **a** CV curves, **b** GCD curves, **c** Ragone plots and **d** cycling performance of the N,S-CQDs/NiCo$_2$S$_4$//N-rGO/Fe$_2$O$_3$ device

anode, and the electrochemical performances, including CV, GCD and EIS, were tested in a voltage window of 0–1.5 V with 2 M KOH solution as electrolyte. Figure 8a displays the CV curves of the as-obtained alkaline aqueous battery at scan rates ranging from 5 to 100 mV s^{-1}, and the shape of CV curves indicates that the capacity originates from the combined contribution of both Faradaic redox reaction and capacitive EDLC at all scan rates. The GCD curves of the alkaline aqueous battery at current densities of 1-20 A g^{-1} are presented in Fig. 8b, and the as-obtained result is further employed to investigate the specific energy (E) and specific power (P) of the alkaline aqueous battery according to the following two formulas [10]: $E = 0.5C(\Delta V)^2/3.6$ and $P = E/t$, where the C, ΔV and t are, respectively, the specific capacity, voltage difference and discharge time of the alkaline aqueous battery. As demonstrated in Ragone plot of Fig. 8c, it is found that the alkaline aqueous battery delivers a superior specific energy of 50.2 Wh kg^{-1} at a specific power of 485 W kg^{-1} and still maintains a decent specific energy of 16.1 Wh kg^{-1} even at an ultrahigh specific power of 9.7 kW kg^{-1}, implying the excellent power

capability. Moreover, the highest specific energy of the assembled alkaline aqueous battery in our work is comparable to or even higher than that of alkaline aqueous devices reported in the literature, including NiCo$_2$O$_4$/CQDs//AC [10], NiCo$_2$S$_4$/NCF//OMC/NCF [32], Ni–Co–S/G//PCN [34], CuCo$_2$O$_4$/CuO//Fe$_2$O$_3$/rGO [56], MnO$_2$/FGS//Fe$_2$O$_3$/FGS [60], Ni(OH)$_2$//AC [65], CF/NiCo$_2$S$_4$@PPy//CF/MoS$_2$ [66], NiCo$_2$S$_4$@G//PC [67], Ni-Co-S@G//RGH [68] and MnO/NCA//Fe$_2$O$_3$/NCA [69]. Additionally, the cycling property of the as-obtained device demonstrated in Fig. 8d was estimated by the GCD measurements at 3 A g^{-1} over 5000 cycles, and 91.5% of capacity retention is maintained, suggesting the superior cycle stability.

The superior electrochemical properties of the N,S-CQDs/NiCo$_2$S$_4$//N-rGO/Fe$_2$O$_3$ device are attributed to the following factors: (1) The utilization of CQDs as structure-directing agents induces the formation of unique N,S-codoped CQDs-decorated urchin-like nanorods-assembled NiCo$_2$S$_4$ microspheres composite. The nanosized building blocks of the composite with a large surface area afford more efficient electroactive sites for charge storage, contributing to

the enhanced specific capacity, and the micrometer-sized assemblies of the composite possess desirable and mechanical properties and superior structure stability, leading to the improved cycling life. Meanwhile, the utilization of CQDs as conductive agents, together with the N,S-codoped modification, greatly enhances the electronic conductivity of the composite, leading to the improvement of rate property; (2) the unique prism-like nanostructured Fe_2O_3 hexahedrons can provide sufficient surface active sites for redox reaction, giving rise to the enhanced specific capacity, and the conductive N-rGO-decorated Fe_2O_3 can significantly boost the electrical conductivity of the composite anode materials, facilitating the fast electron transport kinetic and resulting in the enhanced rate property. Moreover, the Fe_2O_3 hexahedrons are tightly wrapped by the N-rGO layers, which effectively prevents the agglomeration and buffer against the volume change during the charging/discharging cycle process, substantially improving the cycling performance; (3) the ultrahigh-capacity N-rGO/Fe_2O_3 composite anode materials are utilized to couple with the high-performance N,S-CQDs/NiCo$_2$S$_4$ composite cathode materials to fabricate the alkaline aqueous battery, and the rational design and selection of cathode and anode materials render the resulting device achieve the enhanced specific energy, ultrahigh specific power and superior cycling life.

4 Conclusions

In a word, the graphitic CQDs are prepared via a scalable mixed-acid chemical oxidation method employing highly conductive and low-cost Super P powders as precursors, and the high yield of more than 50% is successfully acquired. Then, the resulting CQDs are further used as both structure-directing and conductive agents to controllably synthesize the N,S-codoped CQDs-decorated urchin-like NiCo$_2$S$_4$ composite microsphere cathode materials for the first time, which display evidently improved electrochemical properties including specific capacity, rate performance and cycle life benefited from the synergistic effect of highly conductive N, S-codoped CQDs and unique micro-/nanostructured NiCo$_2$S$_4$ with Faradaic redox feature. Meanwhile, the N-rGO-wrapped prism-like Fe_2O_3 hexahedrons composite anode materials are prepared, which exhibit an ultrahigh specific capacity, substantially enhanced rate performance and cycle property due to the synergistic effect between

highly conductive N-rGO and high-capacity nanostructured Fe_2O_3 hexahedrons. In view of their superior electrochemical properties and rational coupling of cathode and anode materials, a novel alkaline aqueous battery is assembled by employing N,S-CQDs/NiCo$_2$S$_4$ as cathode and N-rGO/Fe_2O_3 as anode in 2 M KOH aqueous electrolyte. The fabricated N,S-CQDs/NiCo$_2$S$_4$//N-rGO/Fe_2O_3 device delivers a high specific energy of 50.2 Wh kg^{-1} at a specific power of 485 W kg^{-1} or an ultrahigh specific power of 9.7 kW kg^{-1} at a decent specific energy of 16.1 Wh kg^{-1} and good cycling life with 91.5% of capacity retention at 3 A g^{-1} over 5,000 cycles. The present research gives a valuable reference for the design and exploitation of superior energy storage devices using battery/capacitive composite materials simultaneously as both cathode and anode in aqueous electrolyte.

References

1. S.Y. Lim, W. Shen, Z. Gao, Carbon quantum dots and their applications. Chem. Soc. Rev. **44**, 362–381 (2015). https://doi.org/10.1039/C4CS00269E

2. R. Das, R. Bandyopadhyay, P. Pramanik, Carbon quantum dots from natural resource: a review. Mater. Today Chem. **8**, 96–109 (2018). https://doi.org/10.1016/j.mtchem.2018.03.003

3. J. Li, X. Yun, Z. Hu, L. Xi, N. Li, H. Tang, P. Lu, Y. Zhu, Three-dimensional nitrogen and phosphorus co-doped carbon quantum dots/reduced graphene oxide composite aerogels with a hierarchical porous structure as superior electrode materials for supercapacitors. J. Mater. Chem. A **7**, 26311–26325 (2019). https://doi.org/10.1039/C9TA08151H

4. X.T. Zheng, A. Ananthanarayanan, K.Q. Luo, P. Chen, Glowing graphene quantum dots and carbon dots: properties, syntheses, and biological applications. Small **11**, 1620–1636 (2015). https://doi.org/10.1002/smll.201402648

5. X. Li, M. Rui, J. Song, Z. Shen, H. Zeng, Carbon and graphene quantum dots for optoelectronic and energy devices: a review. Adv. Funct. Mater. **25**, 4929–4947 (2015). https://doi.org/10.1002/adfm.201501250

6. B. De, N. Karak, Recent progress in carbon dot-metal based nanohybrids for photochemical and electrochemical applications. J. Mater. Chem. A **5**, 1826–1859 (2017). https://doi.org/10.1039/C6TA10220D

7. Y. Wang, A. Hu, Carbon quantum dots: synthesis, properties and applications. J. Mater. Chem. C **2**, 6921–6939 (2014). https://doi.org/10.1039/C4TC00988F

8. Y. Zhu, X. Ji, C. Pan, Q. Sun, W. Song, L. Fang, Q. Chen, C.E. Banks, A carbon quantum dot decorated RuO_2 network: outstanding supercapacitances under ultrafast charge and discharge. Energy Environ. Sci. **6**, 3665–3675 (2013). https://doi.org/10.1039/C3EE41776J

9. J.-S. Wei, H. Ding, P. Zhang, Y.-F. Song, J. Chen, Y.-G. Wang, H.-M. Xiong, Carbon dots/$NiCo_2O_4$ nanocomposites with various morphologies for high performance supercapacitors. Small **12**, 5927–5934 (2016). https://doi.org/10.1002/smll.201602164

10. Y. Zhu, Z. Wu, M. Jing, H. Hou, Y. Yang, Y. Zhang, X. Yang, W. Song, X. Jia, X. Ji, Porous $NiCo_2O_4$ spheres tuned through carbon quantum dots utilised as advanced materials for an asymmetric supercapacitor. J. Mater. Chem. A **3**, 866–877 (2015). https://doi.org/10.1039/C4TA05507A

11. M.-S. Balogun, Y. Luo, F. Lyu, F. Wang, H. Yang, H. Li, C. Liang, M. Huang, Y. Huang, Y. Tong, Carbon quantum dot surface-engineered VO_2 interwoven nanowires: a flexible cathode material for lithium and sodium ion batteries. ACS Appl. Mater. Interfaces **8**, 9733–9744 (2016). https://doi.org/10.1021/acsami.6b01305

12. H. Hou, C.E. Banks, M. Jing, Y. Zhang, X. Ji, Carbon quantum dots and their derivative 3D porous carbon frameworks for sodium-ion batteries with ultralong cycle life. Adv. Mater. **27**, 7861–7866 (2015). https://doi.org/10.1002/adma.201503816

13. C. Ma, K. Dai, H. Hou, X. Ji, L. Chen, D.G. Ivey, W. Wei, High ion-conducting solid-state composite electrolytes with carbon quantum dot nanofillers. Adv. Sci. **5**, 1700996 (2018). https://doi.org/10.1002/advs.201700996

14. L. Zhang, Y. Yang, M.A. Ziaee, K. Lu, R. Wang, Nanohybrid of carbon quantum dots/molybdenum phosphide nanoparticle for efficient electrochemical hydrogen evolution in alkaline medium. ACS Appl. Mater. Interfaces **10**, 9460–9467 (2018). https://doi.org/10.1021/acsami.8b00211

15. X. Xu, R. Ray, Y. Gu, H.J. Ploehn, L. Gearheart, K. Raker, W.A. Scrivens, Electrophoretic analysis and purification of fluorescent single-walled carbon nanotube fragments. J. Am. Chem. Soc. **126**, 12736–12737 (2004). https://doi.org/10.1021/ja040082h

16. X. Yun, J. Li, X. Chen, H. Chen, L. Xiao, K. Xiang, W. Chen, H. Liao, Y. Zhu, Porous Fe_2O_3 modified by nitrogen-doped carbon quantum dots/reduced graphene oxide composite aerogel as a high-capacity and high-rate anode material for alkaline aqueous batteries. ACS Appl. Mater. Interfaces **11**, 36970–36984 (2019). https://doi.org/10.1021/acsami.9b12827

17. Q. Liang, W. Ma, Y. Shi, Z. Li, X. Yang, Easy synthesis of highly fluorescent carbon quantum dots from gelatin and their luminescent properties and applications. Carbon **60**, 421–428 (2013). https://doi.org/10.1016/j.carbon.2013.04.055

18. H. Peng, J. Travas-Sejdic, Simple aqueous solution route to luminescent carbogenic dots from carbohydrates. Chem. Mater. **21**, 5563–5565 (2009). https://doi.org/10.1021/cm901593y

19. A.B. Bourlinos, A. Stassinopoulos, D. Anglos, R. Zboril, M. Karakassides, E.P. Giannelis, Surface functionalized carbogenic quantum dots. Small **4**, 455–458 (2008). https://doi.org/10.1002/smll.200700578

20. R. Liu, D. Wu, S. Liu, K. Koynov, W. Knoll, Q. Li, An aqueous route to multicolor photoluminescent carbon dots using silica spheres as carriers. Angew. Chem. Int. Ed. **48**, 4598–4601 (2009). https://doi.org/10.1002/anie.200900652

21. H. Zhu, X. Wang, Y. Li, Z. Wang, F. Yang, X. Yang, Microwave synthesis of fluorescent carbon nanoparticles with electrochemiluminescence properties. Chem. Commun. **34**, 5118–5120 (2009). https://doi.org/10.1039/B907612C

22. X. Jia, X. Ji, Electrochemical probing of carbon quantum dots: not suitable for a single electrode material. RSC Adv. **5**, 107270–107275 (2015). https://doi.org/10.1039/C5RA24625C

23. T.-Y. Wei, C.-H. Chen, H.-C. Chien, S.-Y. Lu, C.-C. Hu, A cost-effective supercapacitor material of ultrahigh specific capacitances: spinel nickel cobaltite aerogels from an epoxide-driven sol–gel process. Adv. Mater. **22**, 347–351 (2010). https://doi.org/10.1002/adma.200902175

24. G. He, M. Qiao, W. Li, Y. Lu, T. Zhao, R. Zou, B. Li, J.A. Darr, J. Hu, M.-M. Titirici, I.P. Parkin, S, N-Co-doped graphene-nickel cobalt sulfide aerogel: improved energy storage and electrocatalytic performance. Adv. Sci. **4**, 1600214 (2017). https://doi.org/10.1002/advs.201600214

25. Y. Wang, Z. Chen, T. Lei, Y. Ai, Z. Peng, X. Yan, H. Li, J. Zhang, Z.M. Wang, Y.-L. Chueh, Hollow $NiCo_2S_4$ nanospheres hybridized with 3D hierarchical porous rGO/Fe_2O_3 composites toward high-performance energy storage device. Adv. Energy Mater. **8**, 1703453 (2018). https://doi.org/10.1002/aenm.201703453

26. W. Liu, H. Niu, J. Yang, K. Cheng, K. Ye, K. Zhu, G. Wang, D. Cao, J. Yan, Ternary transition metal sulfides embedded in graphene nanosheets as both the anode and cathode for high-performance asymmetric supercapacitors. Chem. Mater.

30, 1055–1068 (2018). https://doi.org/10.1021/acs.chemm ater.7b04976

27. S. Tang, B. Zhu, X. Shi, J. Wu, X. Meng, General controlled sulfidation toward achieving novel nanosheet-built porous square-FeCo$_2$S$_4$-tube arrays for high-performance asymmetric all-solid-state pseudocapacitors. Adv. Energy Mater. **7**, 1601985 (2017). https://doi.org/10.1002/aenm.201601985

28. H. Khani, D.O. Wipf, Iron oxide nanosheets and pulse-electrodeposited Ni–Co–S nanoflake arrays for high-performance charge storage. ACS Appl. Mater. Interfaces **9**, 6967–6978 (2017). https://doi.org/10.1021/acsami.6b11498

29. F. Lu, M. Zhou, W. Li, Q. Weng, C. Li, Y. Xue, X. Jiang, X. Zeng, Y. Bando, D. Golberg, Engineering sulfur vacancies and impurities in NiCo$_2$S$_4$ nanostructures toward optimal supercapacitive performance. Nano Energy **26**, 313–323 (2016). https://doi.org/10.1016/j.nanoen.2016.05.042

30. B.Y. Guan, L. Yu, X. Wang, S. Song, X.W. Lou, Formation of onion-like NiCo$_2$S$_4$ particles via sequential ion-exchange for hybrid supercapacitors. Adv. Mater. **29**, 1605051 (2017). https://doi.org/10.1002/adma.201605051

31. D. Bhattacharjya, A. Sinhamahapatra, J.-J. Ko, J.-S. Yu, High capacity and exceptional cycling stability of ternary metal sulfide nanorods as Li ion battery anodes. Chem. Commun. **51**, 13350–13353 (2015). https://doi.org/10.1039/C5CC0 4289E

32. H. Li, G. Xu, J. Wang, L. Shen, H. Dou, X. Zhang, NiCo$_2$S$_4$ nanosheets grown on nitrogen-doped carbon foams as an advanced electrode for supercapacitors. Adv. Energy Mater. **5**, 1400977 (2015). https://doi.org/10.1002/aenm.201400977

33. Y. Cui, J. Zhang, C. Jin, Y. Liu, W. Luo, W. Zheng, Ionic liquid-controlled growth of NiCo$_2$S$_4$ 3D hierarchical hollow nanoarrow arrays on Ni foam for superior performance binder free hybrid supercapacitors. Small **15**, 1804318 (2019). https://doi.org/10.1002/smll.201804318

34. J. Yang, C. Yu, X. Fan, S. Liang, S. Li, H. Huang, Z. Ling, C. Hao, J. Qiu, Electroactive edge site-enriched nickel–cobalt sulfide into graphene frameworks for high performance asymmetric supercapacitors. Energy Environ. Sci. **9**, 1299–1307 (2016). https://doi.org/10.1039/C5EE03633J

35. D. Li, Y. Gong, C. Pan, Facile synthesis of hybrid CNTs/NiCo$_2$S$_4$ composite for high performance supercapacitors. Sci. Rep. **6**, 29788 (2016). https://doi.org/10.1038/srep29788

36. J. Zhou, C. Booker, R. Li, X. Zhou, T.-K. Sham, X. Sun, Z. Ding, An electrochemical avenue to blue luminescent nanocrystals from multiwalled carbon nanotubes (MWCNTs). J. Am. Chem. Soc. **129**, 744–745 (2007). https://doi.org/10.1021/ja0669070

37. Y. Dong, N. Zhou, X. Lin, J. Lin, Y. Chi, G. Chen, Extraction of electrochemiluminescent oxidized carbon quantum dots from activated carbon. Chem. Mater. **22**, 5895–5899 (2010). https://doi.org/10.1021/cm1018844

38. F. Yuan, T. Yuan, L. Sui, Z. Wang, Z. Xi, Y. Li, X. Li, L. Fan, Z. Tan, A. Chen, M. Jin, S. Yang, Engineering triangular carbon quantum dots with unprecedented narrow bandwidth emission for multicolored LEDs. Nat. Commun. **9**, 2249 (2018). https://doi.org/10.1038/s41467-018-04635-5

39. Y. Si, E.T. Samulski, Synthesis of water soluble graphene. Nano Lett. **8**, 1679–1682 (2008). https://doi.org/10.1021/nl080 604h

40. H. Li, X. He, Z. Kang, H. Huang, Y. Liu, J. Liu, S. Lian, C.H.A. Tsang, X. Yang, S.-T. Lee, Water-soluble fluorescent carbon quantum dots and photocatalyst design. Angew. Chem. Int. Ed. **49**, 4430–4434 (2010). https://doi.org/10.1002/anie.200906154

41. C. Wei, Y. Huang, S. Xue, X. Zhang, X. Chen, J. Yan, W. Yao, One-step hydrothermal synthesis of flaky attached hollow-sphere structure NiCo$_2$S$_4$ for electrochemical capacitor application. Chem. Eng. J. **317**, 873–881 (2017). https://doi.org/10.1016/j.cej.2017.02.130

42. Q. Liu, J. Jin, J. Zhang, NiCo$_2$S$_4$@graphene as a bifunctional electrocatalyst for oxygen reduction and evolution reactions. ACS Appl. Mater. Interfaces **5**, 5002–5008 (2013). https://doi.org/10.1021/am4007897

43. G. Qiuyue, X. Wang, Z. Shi, Z. Ye, W. Wang, N. Zhang, Z. Hong, M. Zhi, Synthesis of porous NiCo$_2$S$_4$ aerogel for supercapacitor electrode and oxygen evolution reaction electrocatalyst. Chem. Eng. J. **331**, 185–193 (2018). https://doi.org/10.1016/j.cej.2017.08.067

44. D. Yuan, G. Huang, D. Yin, X. Wang, C. Wang, L. Wang, Metal-organic framework template synthesis of NiCo$_2$S$_4$@C encapsulated in hollow nitrogen-doped carbon cubes with enhanced electrochemical performance for lithium storage. ACS Appl. Mater. Interfaces **9**, 18178–18186 (2017). https://doi.org/10.1021/acsami.7b02176

45. S. Li, P. Ge, F. Jiang, H. Shuai, W. Xu, Y. Jiang, Y. Zhang, J. Hu, H. Hou, X. Ji, The advance of nickel-cobalt-sulfide as ultra-fast/high sodium storage materials: the influences of morphology structure, phase evolution and interface property. Energy Storage Mater. **16**, 267–280 (2019). https://doi.org/10.1016/j.ensm.2018.06.006

46. Y. Zheng, J. Xu, X. Yang, Y. Zhang, Y. Shang, X. Hu, Decoration NiCo$_2$S$_4$ nanoflakes onto Ppy nanotubes as core-shell heterostructure material for high-performance asymmetric supercapacitor. Chem. Eng. J. **333**, 111–121 (2018). https://doi.org/10.1016/j.cej.2017.09.155

47. S.N. Tiruneh, B.K. Kang, S.H. Kwag, Y. Lee, M. Kim, D.H. Yoon, Synergistically active NiCo$_2$S$_4$ nanoparticles coupled with holey defect graphene hydrogel for high-performance solid-state supercapacitors. Chem. Eur. J. **24**, 1–9 (2018). https://doi.org/10.1002/chem.201705445

48. R. Jia, F. Zhu, S. Sun, T. Zhai, H. Xia, Dual support ensuring high-energy supercapacitors via high-performance NiCo$_2$S$_4$@Fe$_2$O$_3$ anode and working potential enlarged MnO$_2$ cathode. J. Power Sources **341**, 427–434 (2017). https://doi.org/10.1016/j.jpowsour.2016.12.014

49. B. Li, Z. Tian, H. Li, Z. Yang, Y. Wang, X. Wang, Self-supporting graphene aerogel electrode intensified by NiCo$_2$S$_4$ nanoparticles for asymmetric supercapacitor. Electrochim. Acta **314**, 32–39 (2019). https://doi.org/10.1016/j.electacta.2019.05.040

50. Y. Zhu, X. Ji, Z. Wu, Y. Liu, NiCo$_2$S$_4$ hollow microsphere decorated by acetylene black for high-performance

asymmetric supercapacitor. Electrochim. Acta **186**, 562–571 (2015). https://doi.org/10.1016/j.electacta.2015.10.176

51. X. Liang, K. Nie, X. Ding, L. Dang, J. Sun et al., Highly compressible carbon sponge supercapacitor electrode with enhanced performance by growing nickel-cobalt sulfide nanosheets. ACS Appl. Mater. Interfaces **10**, 10087–10095 (2018). https://doi.org/10.1021/acsami.7b19043

52. Y.-M. Fan, Y. Liu, X. Liu, Y. Liu, L.-Z. Fan, Hierarchical porous $NiCo_2S_4$-rGO composites for high-performance supercapacitors. Electrochim. Acta **249**, 1–8 (2017). https://doi.org/10.1016/j.electacta.2017.07.175

53. Y. Shen, K. Zhang, B. Chen, F. Yang, K. Xu, X. Lu, Enhancing the electrochemical performance of nickel cobalt sulphides hollow nanospheres by structural modulation for asymmetric supercapacitors. J. Colloid Interf. Sci. **557**, 135–143 (2019). https://doi.org/10.1016/j.jcis.2019.09.007

54. X. Yun, S. Wu, J. Li, L. Li, J. Zhou, P. Lu, H. Tang, Y. Zhu, Facile synthesis of crystalline $RuSe_2$ nanoparticles as a novel pseudocapacitive electrode material for supercapacitors. Chem. Commun. **55**, 12320–12323 (2019). https://doi.org/10.1039/c9cc06023e

55. Y. Zhu, Z. Huang, Z. Hu, L. Xi, X. Ji, Y. Liu, 3D Interconnected ultrathin cobalt selenide nanosheets as cathode materials for hybrid supercapacitors. Electrochim. Acta **269**, 30–37 (2018). https://doi.org/10.1016/j.electacta.2018.02.146

56. Y. Wang, C. Shen, L. Niu, R. Li, H. Guo, Y. Shi, C. Li, X. Liu, Y. Gong, Hydrothermal synthesis of $CuCo_2O_4$/CuO nanowire arrays and RGO/Fe_2O_3 composites for high-performance aqueous asymmetric supercapacitors. J. Mater. Chem. A **4**, 9977–9985 (2016). https://doi.org/10.1039/C6TA02950G

57. Y. Li, J. Xu, T. Feng, Q. Yao, J. Xie, H. Xia, Fe_2O_3 nanoneedles on ultrafine nickel nanotube arrays as efficient anode for high-performance asymmetric supercapacitors. Adv. Funct. Mater. **27**, 1606728 (2017). https://doi.org/10.1002/adfm.201606728

58. L. Liu, J. Lang, P. Zhang, B. Hu, X. Yan, Facile synthesis of Fe_2O_3 nano-dots@nitrogen-doped graphene for supercapacitor electrode with ultralong cycle life in KOH electrolyte. ACS Appl. Mater. Interfaces **8**, 9335–9344 (2016). https://doi.org/10.1021/acsami.6b00225

59. F. Yang, T. Qiu, C. Chi, S. Liang, L. Deng, X. Wang, C. Wang, J. Fu, Y. Wang, Y. Li, Synergistic effects of nitrogen-doped graphene and Fe_2O_3 nanocomposites in catalytic oxidization of aldehyde with O_2. Chem. Eng. J. **330**, 880–889 (2017). https://doi.org/10.1016/j.cej.2017.08.022

60. H. Xia, C. Hong, B. Li, B. Zhao, Z. Lin, M. Zheng, S.V. Savilov, S.M. Aldoshin, Facile synthesis of hematite quantum-dot/functionalized graphene-sheet composites as advanced anode materials for asymmetric supercapacitors. Adv.

Funct. Mater. **25**, 627–635 (2015). https://doi.org/10.1002/adfm.201403554

61. Y. Zhu, S. Cheng, W. Zhou, J. Jia, L. Yang, M. Yao, M. Wang, J. Zhou, P. Wu, M. Liu, Construction and performance characterization of α-Fe_2O_3/rGO composite for long-cycling-life supercapacitor anode. ACS Sustainable Chem. Eng. **5**, 5067–5074 (2017). https://doi.org/10.1021/acssuschemeng.7b00445

62. Q.X. Low, G.W. Ho, Facile structural tuning and compositing of iron oxide-graphene anode towards enhanced supacapacitive performance. Nano Energy **5**, 28–35 (2014). https://doi.org/10.1016/j.nanoen.2014.01.002

63. X. Xu, W. Shi, P. Li, S. Ye, C. Ye, H. Ye, T. Lu, A. Zheng, J. Zhu, L. Xu, M. Zhong, X. Cao, Facile fabrication of three-dimensional graphene and metal-organic framework composites and their derivatives for flexible all-solid-state supercapacitors. Chem. Mater. **29**, 6058–6065 (2017). https://doi.org/10.1021/acs.chemmater.7b01947

64. Y. Zeng, Y. Han, Y. Zhao, Y. Zeng, M. Yu, Y. Liu, H. Tang, Y. Tong, X. Lu, Advanced Ti-doped Fe_2O_3@PEDOT core/shell anode for high-energy asymmetric supercapacitors. Adv. Energy Mater. **5**, 1402176 (2015). https://doi.org/10.1002/aenm.201402176

65. H.B. Li, M.H. Yu, F.X. Wang, P. Liu, Y. Liang et al., Amorphous nickel hydroxide nanospheres with ultrahigh capacitance and energy density as electrochemical pseudocapacitor materials. Nat. Commun. **4**, 1894 (2013). https://doi.org/10.1038/ncomms2932

66. J. Huang, J. Wei, Y. Xu, Y. Xiao, Y. Chen, A pinecone-inspired hierarchical vertically aligned nanosheet array electrode for high-performance asymmetric supercapacitors. J. Mater. Chem. A **5**, 23349–23360 (2017). https://doi.org/10.1039/C7TA07868D

67. F. Yu, Z. Chang, X. Yuan, F. Wang, Y. Zhu et al., Ultrathin $NiCo_2S_4$@graphene with a core-shell structure as a high performance positive electrode for hybrid supercapacitors. J. Mater. Chem. A **6**, 5856–5861 (2018). https://doi.org/10.1039/C8TA00835C

68. X. Wang, S.-X. Zhao, L. Dong, Q.-L. Lu, J. Zhu, C.-W. Nan, One-step synthesis of surface-enriched nickel cobalt sulfide nanoparticles on graphene for high-performance supercapacitors. Energy Storage Mater. **6**, 180–187 (2017). https://doi.org/10.1016/j.ensm.2016.11.005

69. G. Sun, H. Xie, J. Ran, L. Ma, X. Shen, J. Hu, H. Tong, Rational design of uniformly embedded metal oxide nanoparticles into nitrogen-doped carbon aerogel for high-performance asymmetric supercapacitors with a high operating voltage window. J. Mater. Chem. A **4**, 16576–16587 (2016). https://doi.org/10.1039/C6TA07240B